Acta Geotechnica
https://doi.org/10.1007/s11440-025-02663-2

RESEARCH PAPER

Constrained study of nanoindentation-based upscaling of mechanical properties of shales

Wangxing Cheng[1,2] · Guanglei Cui[1,2] · Derek Elsworth[3] · Yuling Tan[4,5] · Zhejun Pan[6] · Yingjie Guo[1,2] · Yu Zhang[1,2]

Received: 29 November 2024 / Accepted: 10 May 2025

Abstract

Shale gas reservoirs are both heterogeneous and multi-mineralic at microscale, potentially including as many as 10 mineral phases. Mechanical interactions among these different minerals significantly impact gas flow characteristics in matrix and fractures and additionally require transformation to macroscale. We use complementary nanoindentation and triaxial deformation experiments to determine the viscoplastic behavior of the Longmaxi shale at both microscopic and macroscopic scales—and link the two. The distribution of the diverse and heterogeneous mineral microstructure was facilitated by a Tescan integrated mineral analyzer (TIMA). A multi-distance clustering method was used to autonomously differentiate the extensive measured data into mineral groups, with proportions consistent with the XRD results. Pyrite exhibits the highest deformation and creep moduli, followed by dolomite, calcite, quartz then clay. A modified Mori–Tanaka method is applied to upscale the micromechanical properties to macroscale, with results revealing only a minor deviation from the triaxial test. Moreover, a positive correlation was observed between the deformation and creep moduli. The shale reservoir exhibits elastic anisotropy at both micro- and macroscales. Notably, the macroscopic anisotropy ratio is greater than its microscopic counterpart, indicating an increase in anisotropy with an increase in length scale. These findings offer new insights into the mechanical characterization of shale, providing a more comprehensive understanding of its behavior across different scales.

Keywords Elastic anisotropy · Mechanical properties · Nanoindentation · Upscaling

✉ Guanglei Cui
cuiguanglei@mail.neu.edu.cn

[1] State Key Laboratory of Intelligent Deep Metal Mining and Equipment, Northeastern University, Shenyang 110819, China

[2] Key Laboratory of Liaoning Province On Deep Engineering and Intelligent Technology, Northeastern University, Shenyang 110819, China

[3] Department of Energy and Mineral Engineering, G3 Center and Energy Institute, The Pennsylvania State University, University Park, PA 16802, USA

[4] Hebei Research Center of the Basic Discipline Engineering Mechanics, Shijiazhuang Tiedao University, Shijiazhuang 050043, China

[5] Department of Engineering Mechanics, Shijiazhuang Tiedao University, Shijiazhuang 050043, China

[6] State Key Laboratory of Continental Shale Oil, Northeast Petroleum University, Daqing, Heilongjiang 163318, China

Published online: 07 June 2025

1 Introduction

Shale gas resources are important future energy sources due to their abundant reserves, extensive distribution and significant development prospects [12, 63, 75]. Shale gas resources have intricate and varied mineral composition, typically including quartz, feldspars, mica, calcite and other secondary minerals [43]. The mechanical behavior of shale is significantly influenced by the combination of these minerals and their interactions [9, 14]. Specifically, the micromechanical characteristics of shale mineral components are important in modulating microscopic gas flow mechanisms [54, 74] in these intensely pressure-sensitive materials [13, 18]. Understanding mechanical properties is necessary in projecting permeability evolution during drawdown at macroscopic reservoir scale but from limited microscale data. Limited methods exist in linking mechanical to transport properties and in linking these processes across scales.

Shale is a complex sedimentary rock that is mechanically heterogeneous at nanometer scale. Atomic force microscopy (AFM) [25] has been widely used to characterize the heterogeneity of elastic parameters at individual mineral particle scale. Elastic moduli of quartz can reach 70 GPa [30], whereas those for clay minerals may be only one-third of that ($\sim$ 20 GPa) [73]. And indeed, the use of AFM has certain limitations: (i) it is challenging to observe the full range of elastic–plastic phenomena in sampling and (ii) the measured range of moduli is considerably narrower than noted above [29]. To complement this, nanoindentation has been widely employed to probe the mechanical properties of shale at microscale [20, 37, 70]. Nanoindentation can measure both the elastic and creep response of individual mineral phases at the nanoscale. The primary difficulty in this measurement is in linking the numerous measured data points with their corresponding phases [33]. The deconvolution methods have been adopted for the classification of such data points into approximately three or four categories [46]. These studies merely establish the mineral phases of the shale, making it difficult to correlate the numerous data points from nanoindentation with the mineral components.

Conversely, macroscale elastic properties have been widely investigated using uniaxial and triaxial compression testing methods [16]. These analyses reveal that deformation moduli for shale are lower perpendicular to bedding than bedding-parallel. However, these methods depend on macroscale measurements of relatively large intact samples and can only provide composite elastic properties averaged across all constituents and scales of the sample. Another challenge involved in characterizing the behavior of shales lies in its time-dependent characteristics. This is crucial for assessing the healing and sealing behavior of hydraulically induced fractures where the time-dependent response spans multiple length- and time-scales [54–56, 69]. Creep modulus of clays measured by nanoindentation experiments is lower than that for quartz [38] with discrepancies observed between nanoindentation experiments upscaled and those actually measured at macroscale. This is despite statistical correlation between the creep responses measured at the nano- and millimeter scales [39].

Another challenge in applying nanomechanical techniques in shales is in strengthening the connection with macromechanical properties. A comparison of elastic moduli analyzed by acoustic emission and that analyzed by nanoindentation [31] revealed that the correlation coefficient can be as high as 0.97. The Mori-Tanaka approach has been widely employed for homogenizing elastic moduli across scales. Elastic moduli obtained from this improved homogenization method were slightly higher than those obtained from triaxial deformation tests [32]. The much earlier work by Bennett [4] demonstrated instrumented nanoindentation and 3D mechanistic modeling of shale at multiple scales, quantifying the heterogeneity of elastic moduli among constituent minerals. Additionally, the presence of pores, cracks and defects is known to contribute to variations in mechanical properties at different scales [10, 67]. However, these studies and methods often ignore the inherent characteristics of shale mineral components, such as mineral shape and size.

Given these challenges in linking stress and stress-dependent permeabilities across scales, we use careful measurements at micro- and macroscales as a basis for confirming the fidelity of such connections. In contrast, the present study further integrates high-resolution nanoindentation with statistical clustering and a modified Mori–Tanaka upscaling approach to better resolve the contributions of individual mineral phases. Correspondingly, we first measure micromechanical properties of shale, including elasticity and creep. We then link micromechanical properties of minerals with their components before finally developing and confirming a transition in response across scales.

2 Materials and method

We describe nanoindentation experiments coupled with triaxial experiments on the same shale samples together with the theoretical background for the reduction of observations.

2.1 Materials description and preparation

Samples were collected from an outcrop of the Longmaxi formation in the Changning area, Sichuan Province, China (Fig. 1). The Longmaxi formation primarily comprises gray calcareous mudstones [58]. The original cylindrical geometry of the rock core enabled the orientation of the sample to be readily identified (i.e., the bedding plane was horizontal and perpendicular to the axis of the core), as shown in Fig. 1a. Two different loading directions were selected for the evaluation of anisotropy: perpendicular to bedding and parallel to bedding, respectively. Figure 1a presents a schematic illustration of two distinct loading orientations. We use two shale samples, each with a volume of $\sim$ 10 mm^3 (Fig. 1) extracted from the core. The shale exhibits significant anisotropy, with Sample A subjected to perpendicular to bedding plane loading and Sample B subjected to parallel to bedding plane loading. As smooth sample surfaces are crucial for accurate nanoindentation measurements, the upper surfaces were polished using sandpaper progressively ranging from 600 to 7000 grit, followed by mechanical polishing using diamond polishers.

Samples for the triaxial and nanoindentation experiments were collected from the same rock. To prevent any damage to the internal integrity and mechanical properties of the samples, they were wire-cut under anhydrous conditions. Similar to the nanoindentation samples, cylindrical samples with the loading axis aligned in the direction perpendicular and parallel to the bedding plane were prepared, each 25 mm (dia.) $\times$ 50 mm (long). Finally, shale samples with flat and smooth sections were chosen for the experiments.

2.2 Experimental equipment

2.2.1 Nanoindentation

An iMicro nanoindentation system was employed to investigate the micromechanical properties of the shale samples, as shown in Fig. 2. This apparatus consists of three integral components: a nanoindentation instrument, a computer imaging system and an indenter device. The device can withstand a maximum load of 1000 mN, with loading and displacement accuracies of 6 nN and 0.05 nm, respectively, with minimal thermal drift. The device ensures high-resolution across its entire spectrum using an electromagnetic drive-based loading force exciter and a three-piece capacitive sensor design known for its high sensitivity. Prior to nanoindentation testing, the surfaces of the samples were scanned for roughness to evaluate their suitability for testing. In all cases, a surface roughness < 70 nm across an area of 80 μm was considered sufficient for performing the nanoindentation test [62].

2.2.2 Triaxial system

A multi-coupled triaxial system was used to determine the macroscopic mechanical properties of the shale. The experimental apparatus consists of three principal components, namely, a pressure chamber, a servo-pressure pump and a control system. Pressures are measured with an accuracy of $\pm$ 0.25%. Confining pressure of 100 MPa and axial pressure of 780 kN can be applied simultaneously with sample deformations measured to an accuracy of 0.1%.

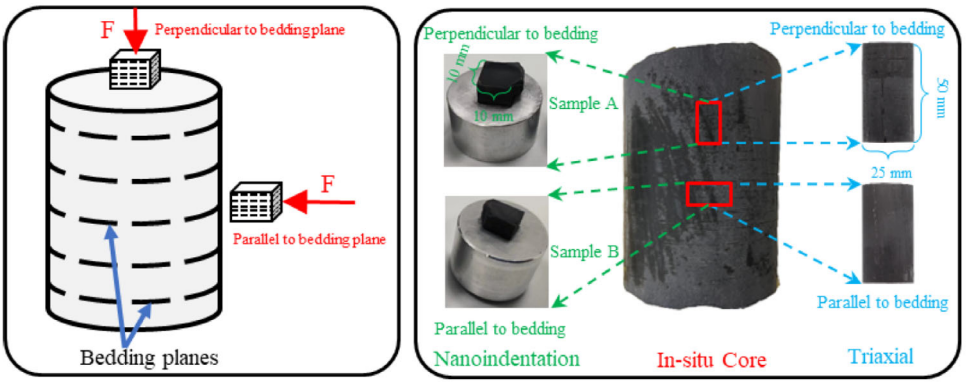

(a) (b)

Fig. 1 **a** Illustration of two differently oriented samples for nanoindentation testing (F: indentation load); **b** Experimental sample preparation: (Left) Nanoindentation test samples, and (Right) Triaxial test samples. *Note* Perpendicular and parallel refer to the loading angle relative to the bedding direction

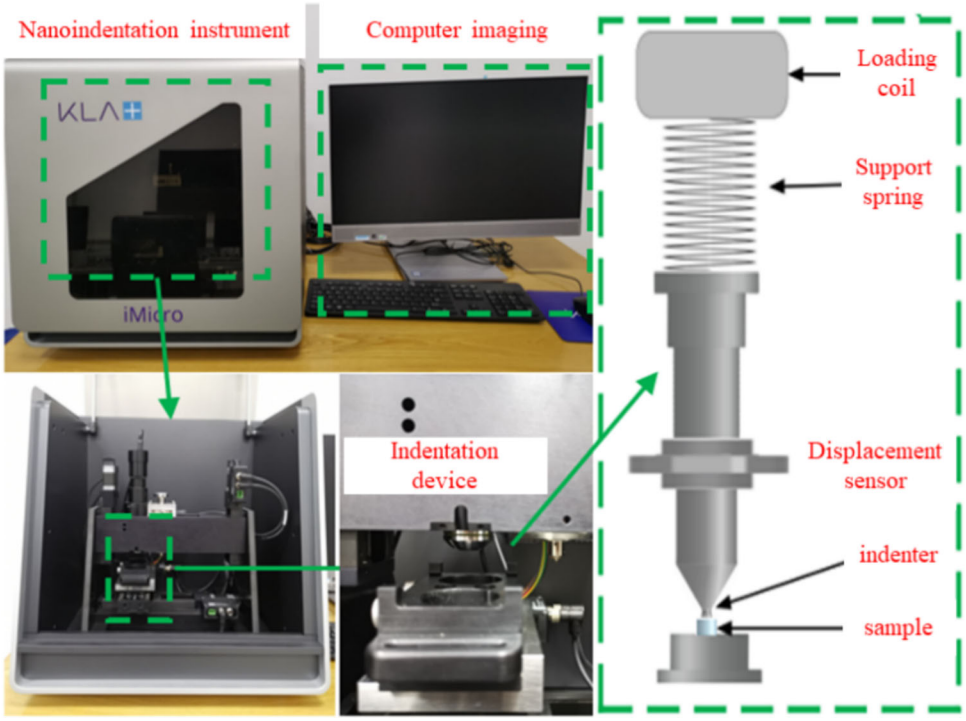

Fig. 2 iMicro nanoindentation system for the measurement of shale micromechanical properties

2.2.3 Microscale mineralogic characterization

After completion of all nano-characterization measurements, the mineral composition of the samples was determined using an X-ray diffractometer. The microstructure of shales were analyzed using a Tescan integrated mineral analyzer (TIMA), comprising four EDAX Element 30 spectroscopic probes and reduced with TIMA automatic processing software (Fig. 3). Gray scales of the backscattered images were adjusted to distinguish among different mineral phases. Subsequently, energy spectrum probes were employed to obtain substantial data on the composition of the elements. Observations were automatically processed to compare energy spectra of the unknown minerals with known standards. All the data were integrated and consolidated.

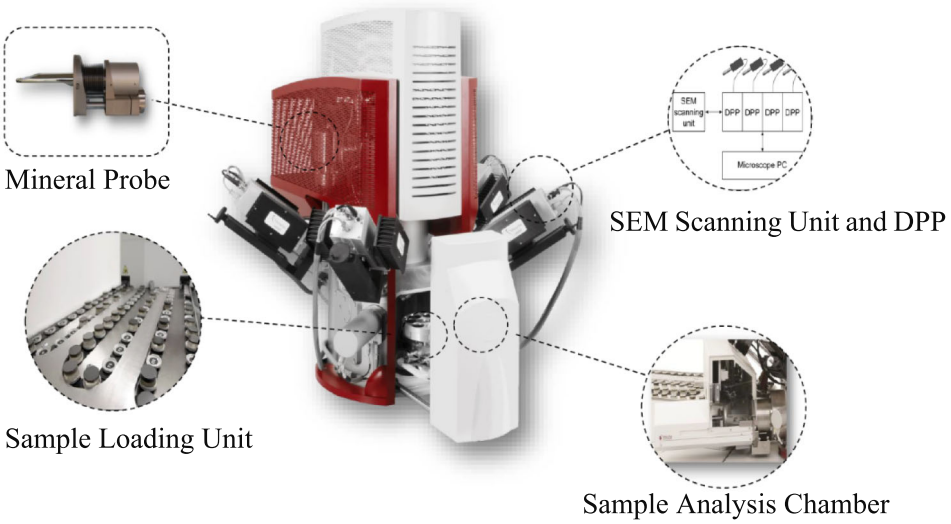

Fig. 3 Tescan integrated mineral analyzer

2.3 Experimental methods

2.3.1 Mineral micromechanical testing

The shale samples were indented at constant temperature using the iMicro nanoindentation instrument. A minimum of 100 indentations were conducted on each of two sample surfaces. The tip area function was calibrated by performing indentation tests to various contact depths on standard samples to ensure the accuracy of the nanoindentation. Indentation depths ranged from approximately 100 nm to 1000 nm, which are sufficiently smaller than the typical mineral grain size and are well above the measured surface roughness (< 70 nm). This ensures that the indentation response predominantly reflects the intrinsic properties of the individual mineral phases. As shown in Fig. 4a, the nanoindentation testing was conducted on a 10×10 grid with a 50 μm spacing between each indentation to minimize potential mechanical interference from neighboring indentations. All nanoindentation tests were conducted in load-control mode with a loading rate of 1 mN/s and an unloading rate of 1 mN/s, so that the maximum load was reached in approximately 5 s and the unloading was completed within 5 s. These rates were selected based on instrument calibration and literature precedent to minimize the influence of viscous effects. Nanoindentation testing was performed in load-control mode with a peak load of 5 mN and a holding time of 120 s. Figure 4b shows a typical nanoindentation load–hold–unload curve.

2.3.2 Macromechanical testing

Differential-stress creep data were collected from individual shale specimens using incremental enhancement in differential stress. Table 1 presents the specific differential stress and the magnitude of the confining pressure. The triaxial creep experiment was conducted using the following steps: first, the shale samples were placed in a core holder within a jacket; secondly, the heat-shrink sleeves were heated to seal the sample and rubber rings were adjusted to secure the ends; and finally, displacement sensors were installed at specific points for monitoring the deformation. Meanwhile, to achieve the stress conditions specified in Table 1, a peripheral pressure of 15 MPa was initially applied at a rate of 1 MPa per minute, followed by the application of an incremented differential stress. Upon reaching the desired stress levels, the test commenced and deformations were recorded with time. This procedure was carefully repeated for each sample to complete the creep experiments according to the conditions presented in Table 1.

2.4 Data reduction methods

2.4.1 Micromechanical parameters

Nanoindentation refers to a precise method for investigating the nanoscale mechanical properties of materials. This technique involves a specialized probe that contacts the sample surface and measures penetration depth with applied load [25]. As shown in Fig. 4b, the indentation curve can be divided into three distinct stages: loading, holding and unloading. The micromechanical properties of the shale are calculated based primarily on the assumption of the elastic deformation observed during the final unloading stage [51]. We acknowledge that the presence of viscoplastic behavior may affect the initial unloading slope; however, the adopted method is widely employed [33, 36, 50, 68] as the affect can be ignored, and

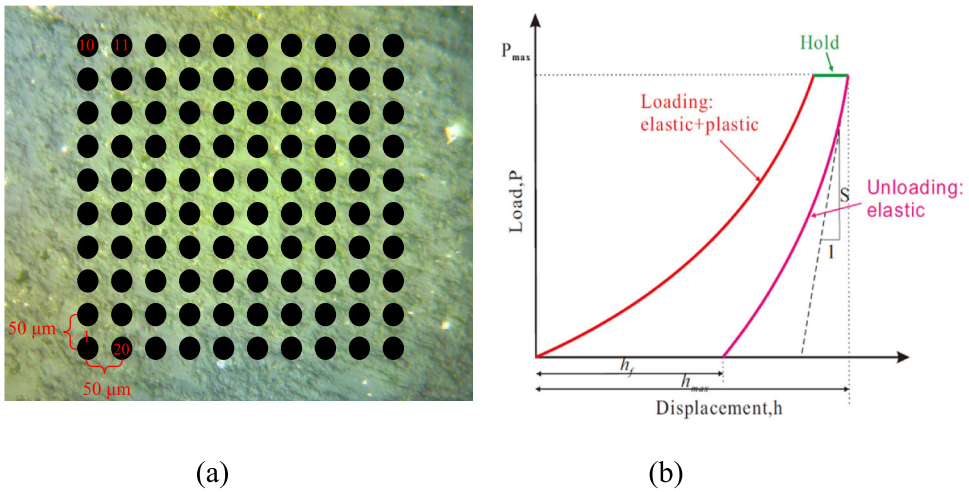

Fig. 4 **a** A typical indentation grid. **b** Indentation load–displacement curve [23]

Table 1 Confining pressure and axial stress applied to the shale sample

Loading angle with respect to bedding	Confining pressure (MPa)	Differential pressure (MPa)		
Parallel	15	20	40	60
Perpendicular	15	20	40	60

complementary creep tests were performed to characterize the time-dependent response.

During the unloading stage, modulus can be defined as

$$\frac{1}{E_r} = \frac{1-v^2}{E} + \frac{1-v_i^2}{E_i} \tag{1}$$

where v is Poisson's ratio; v_i is Poisson's ratio of the Berkovich indenter; and E_i is the elastic indentation modulus of the Berkovich indenter. E_r indicates the reduced modulus, which can be calculated as:

$$E_r = \frac{\sqrt{\pi}S}{2\sqrt{A_c}} \tag{2}$$

where A_C represents the contact area, and S refers to the contact stiffness. These terms are calculated as follows:

$$A_c = 24.5h_c^2 \tag{3}$$

$$S = \left(\frac{dP}{dh}\right)_{h_{\max}} \tag{4}$$

Finally, the hardness is determined using Eq. (5).

$$H = \frac{P_{\max}}{A_c} \tag{5}$$

2.4.2 Creep characteristics

In both nanoindentation and triaxial creep tests, displacements exhibited an approximate logarithmic variation with time. Therefore, we employed Eq. 6, as recommended by Mighani [46] to represent the creep results.

In nanoindentation, creep is expressed as [59, 64]:

$$h(t) - h_0 \approx x_1 \ln(t - t_0 + 1) \tag{6}$$

where is the indenter depth, x_1 is a constant and t_0 and h_0 are the time and depth at the start of the hold, respectively.

The creep compliance rate of change is expressed as:

$$\dot{L}(t) = \frac{2a(t)\dot{h}(t)}{P} \approx \frac{2a_U\dot{h}(t)}{P} \tag{7}$$

where $a(t)$ is the effective contact radius and P is the constant loading.

During the holding of the load for 120 s, given that the increase in contact radius is less than 10%, $a(t)$ can be expressed in terms of the contact radius, a_u. Equations. (6) and (7) provide the following result [65]:

$$\dot{L}(t) \approx \frac{1}{Ct} \tag{8}$$

where C refers to the creep modulus, which characterizes the nanoindentation creep behavior, and can be described as:

$$C = \frac{P}{2a_U x_1} \tag{9}$$

For the triaxial tests, the creep behavior can be described by Eq. (10) [38]:

$$\varepsilon(t) - \varepsilon(0) = y_1 \ln(t - t0 + 1) \tag{10}$$

where $\varepsilon(0)$ refers to creep strain at the start of the holding step, and $\varepsilon(t)$ represents the creep strain value at time t.

Creep compliance can be expressed as:

$$\dot{L_j}(t) = \frac{\dot{\varepsilon}(t)}{\sigma} = \frac{1}{C_t t} \tag{11}$$

where σ indicates the loading.

Combining Eqs. (10) and (11), the creep modulus can be expressed as [38]:

$$C_t = \frac{\sigma}{y_1} \tag{12}$$

2.4.3 Micromechanical properties of minerals

The nanoindentation experiments revealed that the mechanical parameters did not follow a strictly normal distribution but instead exhibited an overlay of multiple normal probability density functions. Accordingly, multivariate clustering analysis was employed to separate the discrete distributions. The nanoindentation data comprised numerous distinct mechanical components, each of which followed a normal distribution. Therefore, the experimental data should conform to a Gaussian mixture model (GMM) [17]. During the clustering analysis, modulus and hardness were selected as multivariate variables for data analysis. Model convergence was performed by optimizing the model parameters using the expectation–maximization algorithm [15, 44].

GMM assumes that data points are drawn from a mixture of k Gaussian distribution functions with unknown parameters. The model can be expressed as:

$$p(x_i) = \sum_{j=1}^{k} f_j c\left(x_i; \mu_j, \Sigma_j\right) \tag{13}$$

where x_i is a data point, k is the number of Gaussian functions, f_i represents the mixing weight of the j-th Gaussian distribution function, and μ_i and Σ_j refer to the mean and covariance matrix, respectively.

The multivariate normal density function for an observation x_i from the j-th cluster is defined as:

$$c\left(x_i;\mu_j,\Sigma_j\right)=\frac{1}{(2\pi)^{d/2}}\left|\Sigma_j\right|^{-\frac{1}{2}}\exp^{-\frac{1}{2}\left(x_i-\mu_j\right)^T\Sigma_j^{-1}\left(x_i-\mu_j\right)} \tag{14}$$

where d indicates the data dimension and $|\Sigma_j|$ is the determinant.

The EM algorithm for estimating the GMM parameters involves two steps [48]. The first step is the expectation step (E-step), where the posterior probability of each data point belonging to each Gaussian distribution function is calculated as:

$$\gamma_i(z_i=j)=\frac{f_j c\left(x_i;\mu_j,\Sigma_j\right)}{\Sigma_{l=1}^{k} f_l c\left(x_i;\mu_j,\Sigma_j\right)} \tag{15}$$

The second step is the maximization step, where the model parameters are updated to maximize the log-likelihood function given by:

$$f_i=\frac{1}{N}\sum_{i}^{N}\gamma_i(z_i=j) \tag{16}$$

$$\mu_i=\frac{\sum_{i=1}^{N}\gamma_i(z_i=j)x_i}{\sum_{i=1}^{N}\gamma_i(z_i=j)} \tag{17}$$

$$\sum\nolimits_j=\frac{\sum_{i=1}^{N}\gamma_i(z_i=j)\left(x_i-\mu_j\right)\left(x_i-\mu_j\right)^T}{\sum_{i=1}^{N}\gamma_i(z_i=j)} \tag{18}$$

where N refers to the number of data points.

By iteratively performing the E-step and M-step, the EM algorithm progressively optimizes the parameters until convergence. The above method was implemented using the sklearn.mixture routine in Python.

2.4.4 Upscaling methods

In this study, a homogenization method was employed in the upscaling. The Mori–Tanaka method is the most commonly employed approach for homogenization of elastic mechanical properties. This method assumes that each composite comprises multiple inclusions with varying properties, thereby approximating the interaction between components. This assumption aligns with the inherent nature of the shale. Additionally, a fourth-order tensor was employed for the characterization of strain [49]. Based on this concept, the bulk modulus and shear modulus of shale composed of n components can be represented as:

$$K_{\text{hom}}=\frac{\sum_{J=1}^{n} f_J\cdot K_J(1+\alpha_0\cdot(K_J/K_0-1))^{-1}}{\sum_{J=1}^{n} f_J\cdot(1+\alpha_0\cdot(K_J/K_0-1))^{-1}} \tag{19}$$

$$G_{\text{hom}}=\frac{\sum_{J=1}^{n} f_J\cdot G_J(1+\beta_0\cdot(G_J/G_0-1))^{-1}}{\sum_{J=1}^{n} f_J\cdot(1+\beta_0\cdot(G_J/G_0-1))^{-1}} \tag{20}$$

where K_0 and G_0 represent the bulk modulus and shear modulus of the reference medium, respectively. f_J indicates the volume fraction of the J_{th} phase. α_0 and β_0 refer to the microstructural parameters.

Conventional upscaling methods often overlook the influence of mineral shape on microstructural parameters. This, in turn, affects the macroscopic elastic modulus of the overall composite. Here, the shape factor maps the impact of particle morphology on the behavior of the mineral within the composite system. As a result, a shape factor-based correction factor was incorporated into the microstructural parameters, which represents the effect of the nonideal shape of the inclusion body on the elastic field. This is expressed as:

$$\alpha_J=S_J\frac{3K_0}{3K_0+4G_0} \tag{21}$$

$$\beta_J=S_J\frac{6K_0+12G_0}{15K_0+20G_0} \tag{22}$$

where S_J is the weighted shape factor of the mineral in the Jth phase. This factor is calculated using the built-in analysis module in Avizo (an image analysis software), which directly measures the particle morphology from TIMA images. This factor represents an inherent property of the mineral inclusion's geometry and is used to correct the elastic field in the MT method. It is not treated as a fitting parameter but as a measured value that accounts for the nonideal shape of the inclusions, thereby enhancing the robustness of the upscaling procedure.

Incorporating Eqs. (21) and (22) into Eqs. (19) and (20), respectively, results in

$$K_{\text{modified}}=\frac{\sum_{J=1}^{n} f_J\cdot K_J(1+\alpha_J\cdot(K_J/K_0-1))^{-1}}{\sum_{J=1}^{n} f_J\cdot(1+\alpha_J\cdot(K_J/K_0-1))^{-1}} \tag{23}$$

$$G_{\text{modified}}=\frac{\sum_{J=1}^{n} f_J\cdot G_J(1+\beta_J\cdot(G_J/G_0-1))^{-1}}{\sum_{J=1}^{n} f_J\cdot(1+\beta_J\cdot(G_J/G_0-1))^{-1}} \tag{24}$$

The classical Mori–Tanaka method is applied based on the volume fractions, elastic moduli and shape factors of the identified mineral phases. Although some studies [4] describe shales as having an 'organic/clay matrix' with hard inclusions, in this work the clay phase—comprising minor organic matter—is treated as a single entity. Consequently, the upscaling process via the MT method remains robust, as any local variations due to organic content are averaged in the statistical analysis. Ultimately, this set of equations allows for the homogenization of elastic properties, such as modulus. We utilize these relations to effectively combine the mechanical characteristics of different phases to derive an overall description of the behavior of composite material [49]

$$E_{\text{hom}} = \frac{9K_{\text{modified}}G_{\text{modified}}}{3K_{\text{modified}} + G_{\text{modified}}} \tag{25}$$

3 Results

We analyze the experimental data for three components: (1) shale mineral composition and microstructure, (2) micromechanical properties and (3) macroscopic mechanical properties.

3.1 Shale mineral composition and microstructure

The quantitative results of the XRD analysis of the sample are presented in Table 2. The sample comprises predominantly calcite, dolomite, pyrite, quartz and clay minerals. Due to the low crystallinity of clay minerals, their signature in the XRD spectrum appears as a broad hump rather than distinct peaks. To estimate the clay content, the proportions of well-defined crystalline phases (e.g., quartz, calcite, dolomite and pyrite) were first determined from their individual peaks. The clay mineral content was then determined as 100% minus the sum of these identifiable phases. This approach is widely employed in XRD analyses of shales [8, 45]. Notably, carbonates (calcite and dolomite) constitute a significant portion of the sample, accounting for $\sim$ 50 wt%. The clay content determined in the present study ($\sim$ 15 wt%) is lower than typical values reported for typical shales reservoirs. This discrepancy may be attributed to the specific depositional environment and diagenetic history of the Longmaxi shale in the Changning area [7, 40]. Similar low clay contents have also been reported in other studies of Longmaxi shale [7, 35, 71].

TIMA was employed to examine shale microstructure. The mineral surface distribution was examined in the two distinct loading directions. The minerals in shale exhibit significant variability, with Table 3 presenting the volume fraction of each mineral. Quartz constitutes a significantly higher volume fraction compared to other minerals. The proportions of dolomite, calcite and clays are almost equivalent on perpendicular loading and parallel loading, with relative to the bedding. The proportion of pyrite is significantly higher for loading perpendicular to bedding. Mineral particle size distribution was investigated based on mineral volume fractions. The particle size distribution of carbonate minerals and clay minerals demonstrates no particular difference in the two directions. Quartz indicates a significantly higher peak value on planes in the bedding-perpendicular loading direction relative to the bedding-parallel loading direction. When compared to quartz, the particle sizes of pyrite are significantly smaller on planes in the bedding-perpendicular loading relative to the bedding-parallel loading direction. This accommodates the varying shapes of shale minerals in divergent bedding directions, suggesting the anisotropic nature of mineral mechanical properties. Additionally, it indicates the need for considering mineral grain size during upscaling.

3.2 Micromechanical properties

Under identical maximum loads, the range of maximum indentation depths varies with the loading direction. When loaded perpendicular to bedding, depths range from 100 to 700 nm, whereas loading parallel to bedding extends from 100 to 1000 nm.

Nanoindentation experiments were performed to assess the modulus and indentation strength of shale at the

Table 2 Mineral composition of the Longmaxi shale

	Quartz	Clay minerals	Carbonate minerals		Pyrite
			calcite	dolomite	
Longmaxi shale	34%	15.3%	25.4%	22.2%	1.7%

Table 3 Volume fraction of each mineral in the shale

Primary phase	Parallel to bedding (%)	Perpendicular to bedding (%)
Quartz	53.04	49.74
Calcite	13.88	17.89
Dolomite	11.94	11.51
Clay	12.53	9.34
Pyrite	0.29	5.50

microscopic level. Figure 5 illustrates minimal variation in results across different loading angles at this scale. This can be attributed chiefly to the relatively small size of the probe compared to the mineral particles and the adequately large number of probing points sampling all mineral components within the shale.

Figure 6 displays a box plot of modulus and hardness obtained from nanoindentation of the shale. The main distribution ranges of modulus and hardness vary noticeably under different loading directions. For loading perpendicular to the bedding, modulus and hardness range primarily from 51.12 to 69.66 GPa and 2.16 to 4.64 GPa, respectively. Conversely, loading parallel to the bedding results in modulus and hardness ranging mainly from 54.02 to 75.07 GPa and 1.91 to 4.39 GPa, respectively. Additionally, the distribution of modulus values approximates a normal profile. The hardness value is more concentrated around the median, likely because of the nonlinear dependence of hardness on the underlying microstructure. Both distributions can be represented by a superposition of multiple probability density functions, forming the basis for the hypotheses of clustering analysis.

3.3 Triaxial strains

Creep strain measurements were obtained from triaxial compression tests for samples subjected to different levels of differential stress in both parallel loading and perpendicular loading, relative to the bedding directions, as illustrated in Fig. 7. The samples exhibit noticeable creep behavior. Additionally, creep under perpendicular loading to the bedding is generally larger than that under parallel loading, consistent with findings reported by Sone [61].

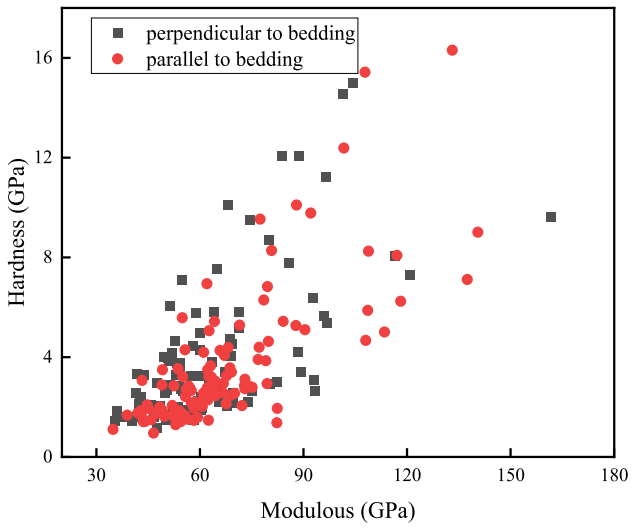

Fig. 5 Nanoindentation test results measured loading on planes bedding-perpendicular (black) and bedding-parallel (red)

This difference may be attributed to the sedimentary nature of shale, where bedding planes or interlayer cracks tend to close more under vertical stress, resulting in reduced mechanical properties and more pronounced creep behavior. Moreover, as the differential stress increases, the magnitude of creep also increases significantly.

4 Discussion

We explore the relationship between micromechanical parameters of shale and its components, together with an investigation into the use of logarithmic functions in fitting shale creep. Additionally, a comparative analysis is conducted to examine mechanical correlations between micro- and macroscales, contrasting with previous research.

4.1 Clustering analysis

4.1.1 Relationship between modulus and mineral phase

The morphology of load–displacement curves allows distinction between various mechanical phases [3]. Under identical loading, a larger indentation depth is typically exhibited by a soft phase compared to a hard phase. However, this serves merely as an initial approximation for the mechanical analysis and classification of minerals. Differentiation among the various mechanical phases associated with each shale was attempted using a Gaussian mixture model.

Initially, Python data analysis software processed the indentation data, collating the total number of phases in the composite. Following this, a multivariate statistical approach differentiated mechanical phases within each cluster based on their modulus and hardness characteristics. To validate the findings, separate cluster analyses were conducted for datasets representing each loading direction, as depicted in Fig. 8.

Table 4 also shows specific phase percentages. Notably, in the cluster analysis, quartz percentages exceeded by 14% and 9%, and clay percentages exceeded by 1% and 8%, respectively, compared to the XRD results. This deviation may stem from a mixture of quartz and clay matrix presence at the shale interface, causing indentation measurement discrepancies. Note that while the clay phase may contain organic matter [34], our analysis does not independently quantify organic content; rather, the clay's mechanical response reflects the combined properties of clay and its entrained organics.

By employing a Gaussian mixture model to analyze shale micromechanics and integrating XRD data, we clarified how micromechanical parameters relate to mineral composition. This sets the stage for a deeper exploration of

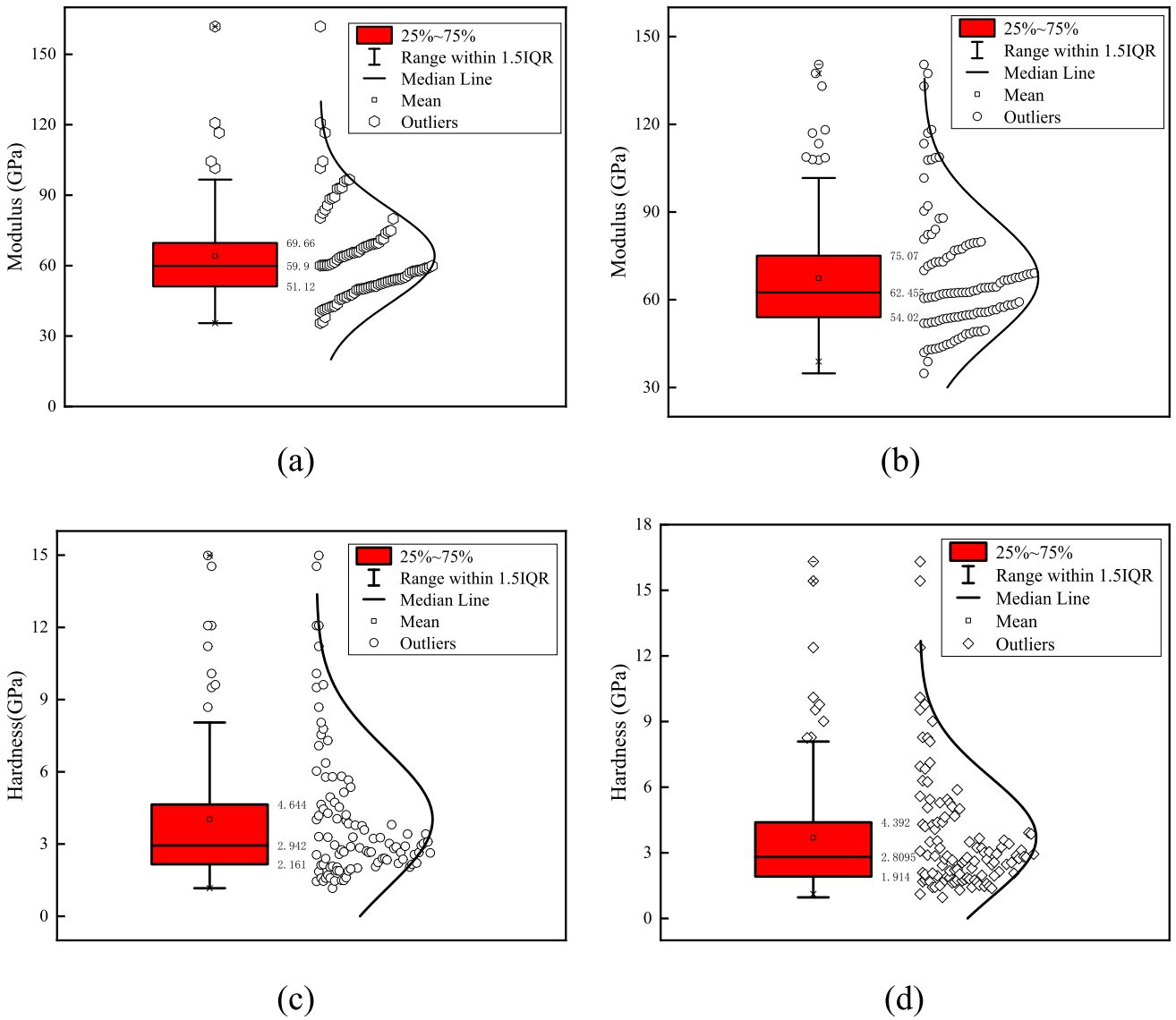

Fig. 6 Box plot and normal distribution curves for shale. **a** and **c** are loaded perpendicular to bedding; **b** and **d** are loaded parallel to bedding

the connection between the micro- and macromechanical properties of shale.

4.1.2 Dependence of creep strain on the logarithm of time

Clustering techniques reveal groups of nanoindentation characteristics within the Longmaxi shale samples. These clusters frequently align with quartz and clay, showing minimal overlap with pyrite—a distinguishing characteristic of shale. Particularly noteworthy are moduli exceeding 50 GPa observed in individual indentations on clay materials, indicating that the clay cluster may represent regions with relatively lower organic matter content within the clay matrix.

Using clustering techniques on data points in the modulus-creep compliance space, we identify five distinct nanoindentation groups (refer to Fig. 9). The softest indentations were mainly found within the clay matrix background, forming a well-defined and compact group (located in the upper-left cluster in Fig. 9). In contrast, the hardest group consisted of indentations with the highest modulus values and lowest creep compliance values. An exponential trend is observed in the average values of creep compliance with increase in modulus, although significant variability exists within each phase. However, creep compliance values showed minimal variation with increase in rock strength. Additionally, there was noticeable anisotropy in creep compliance, with higher values observed in parallel loading relative to the bedding compared to perpendicular loading relative to the bedding orientations.

In the previous section, we established a correlation between creep compliance and the mineralogical

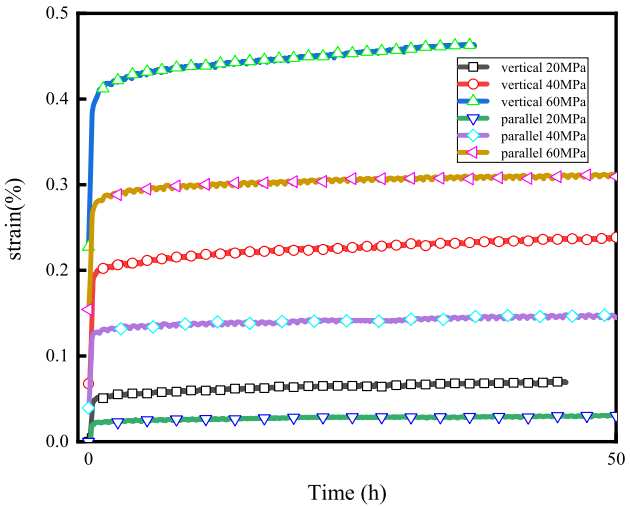

Fig. 7 Creep strains of shale samples under various differential stresses

composition of shale. We utilized a logarithmic function model to effectively fit the shale creep curves. As shown in Fig. 10, various mechanical phases observed in nanoindentation experiments were successfully modeled with correlation coefficient (R^2) values exceeding 0.9. Notably, the correlation coefficient for pyrite under loading perpendicular bedding is 0.546. During nanoindentation on mineral surfaces, pyrite, being a surface material, directly interfaced with the indenter, causing underlying material beneath the pyrite—without direct contact with the indenter—to fracture. This resulted in a sudden increase in indentation depth in the later part of the creep curve. This behavior suggests a logarithmic increase in indentation depth with increase in holding time, indicating time-dependent deformation. The varying indentation creep depths at different loading angles provide additional insights into the anisotropic characteristics of shale minerals.

Table 4 Clustering analysis for the shale

Sample	Quartz	Clay	Carbonate minerals		Pyrite
			calcite	dolomite	
A	43%	23%	16%	15%	3%
B	48%	16%	16%	19%	1%

According to Eq. 9, both x_1 and P_{max} remain constant throughout the entire creep process for each indentation. We determined the creep modulus of each indentation at a creep time (120 s). Nanoindentations exhibited significant spatial variability in E (modulus), H (hardness) and C (creep modulus), with values ranging from 30 to 160 GPa, 1 to 16 GPa and 10^4 to 10^7 GPa, respectively.

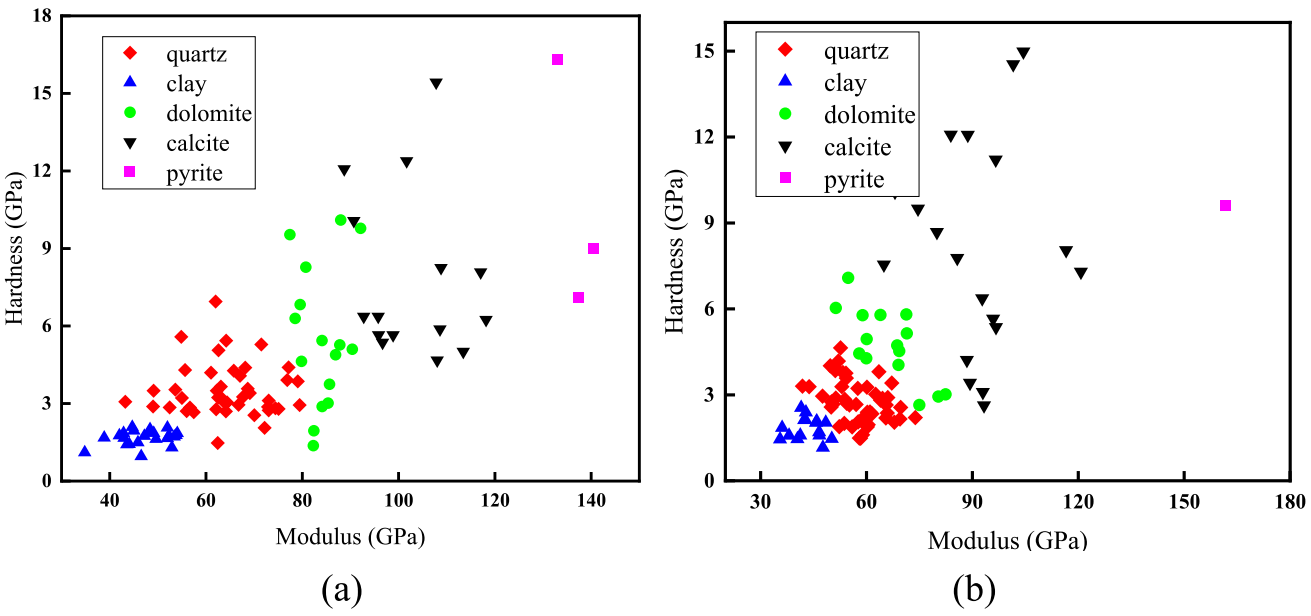

Fig. 8 Nanoindentation clustering analysis for the shale sample. **a** parallel loading relative to the bedding; **b** perpendicular loading relative to the bedding

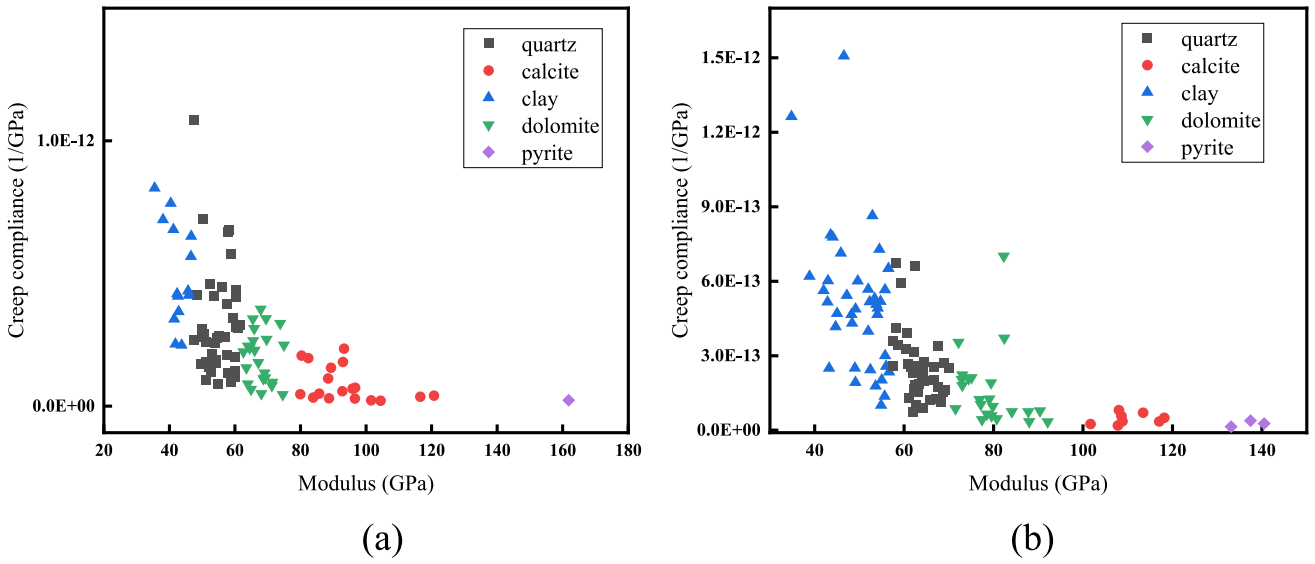

Fig. 9 Creep compliance measured in nanoindentation creep tests, **a** bedding-perpendicular loading; **b** bedding-parallel loading

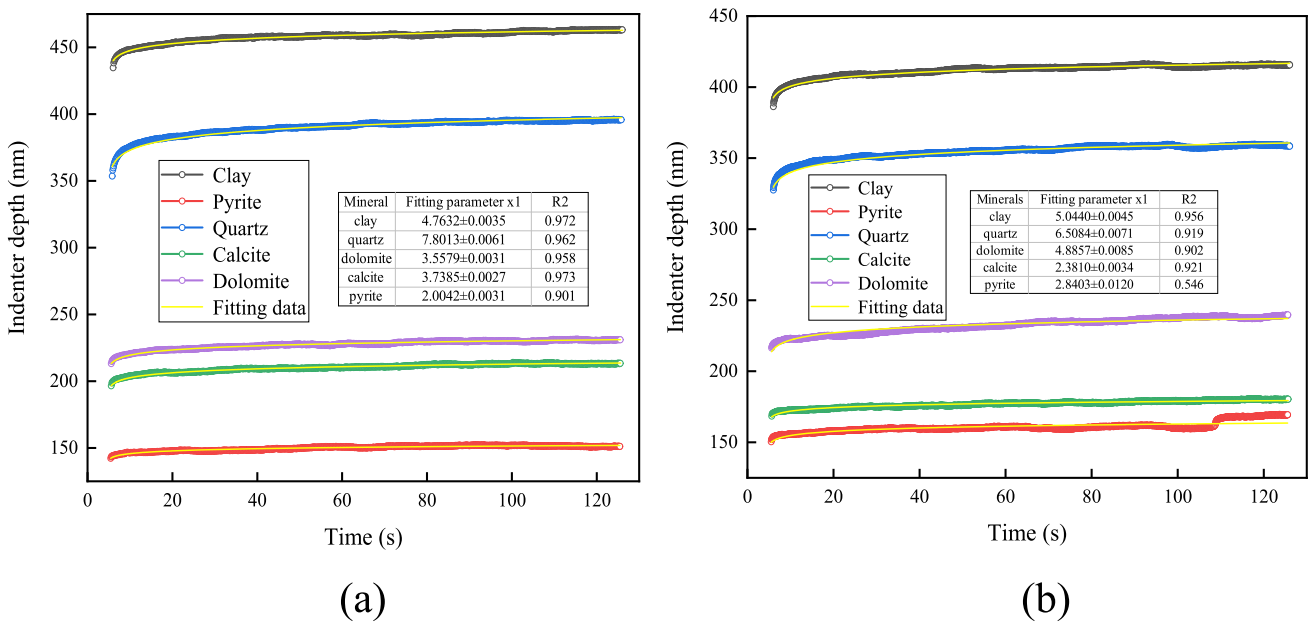

Mineral	Fitting parameter x1	R2
clay	4.7632±0.0035	0.972
quartz	7.8013±0.0061	0.962
dolomite	3.5579±0.0031	0.958
calcite	3.7385±0.0027	0.973
pyrite	2.0042±0.0031	0.901

Minerals	Fitting parameter x1	R2
clay	5.0440±0.0045	0.956
quartz	6.5084±0.0071	0.919
dolomite	4.8857±0.0085	0.902
calcite	2.3810±0.0034	0.921
pyrite	2.8403±0.0120	0.546

Fig. 10 Curve fitting of the creep data of different mechanical phases, **a** bedding-perpendicular loading; **b** bedding-parallel loading

4.2 Linkage of mechanical properties between micro- and macroscales

4.2.1 Elasticity upscaling

To refine the mechanical parameters of shale more precisely, increasing the number of indentations on the same rock surface is crucial. Nanoindentation results highlight significant variations in mechanical properties across different minerals within a single sample. The approach combines cluster analysis with XRD findings, treating the rock as a composite material composed of phases of quartz, clay, calcite, dolomite and pyrite. By integrating volume fractions of these phases and applying a compositional mechanical model, mechanical properties of the bulk rock can be determined, scaling up from the nanoscale to the centimeter scale. Utilizing the Mori–Tanaka method facilitates upscaling mechanical parameters from nano to micro scales, also enabling a transition strategy from micro to macro mechanical scales. To validate the accuracy of the upscaling model, results are compared with macroscopic modulus tests performed on shale.

Table 5 presents the mechanical parameters obtained through three different approaches. It is observed that the

Table 5 Upscaling elastic modulus results

Loading Angle	Modulus in compression test/GPa	Scale-up models considering shape factors/ GPa	Scale-up models without considering shape factors /GPa
Perpendicular bedding	24.4	30.4	33.6
Parallel bedding	30.3	33.4	36.1

values calculated using the scale-up model are closely aligned with those from triaxial compression tests. Nonetheless, the elastic modulus of the macroscopic sample is found to be lower compared to that of the scaled-up model. This variation is primarily attributed to differences in mechanical properties at various scales, mainly due to the presence of natural micropores and cracks, which are more evident in larger test samples. As the load increases, these natural weak defects may cause the propagation of cracks, resulting in the development of interconnected fractures, thus reducing the elastic mechanical properties of shale.

Furthermore, when the shape factor of the minerals is considered, the homogenized elastic modulus more accurately reflects the macroscopic sample scale. This underscores the importance of integrating nanoindentation with mineral mapping techniques on the rock surface to precisely assess the mechanical properties of each phase. Moreover, the impact of the mineral shape and size must be taken into account to establish a more accurate correlation between the micro- and macroscales.

4.2.2 Comparison between nanoindentation and triaxial tests

The creep modulus of shale, derived from nanoindentation experiments, ranges between 10^4 and 10^7 GPa. These findings are consistent with the creep modulus values ranging from 10 to 10^7 GPa reported by Mighani et al. [46].

An understanding of the creep properties of each indentation facilitates the estimation of the creep modulus using a micromechanical-based homogenization scheme. It is assumed that the indented areas of each sample, comprising 100 equal-volume fractions, are randomly distributed. Shale may exhibit either viscoelastic or viscoplastic behavior, thus necessitating accurate assumptions during the modeling of results. A self-consistent scheme [22] was utilized to estimate the creep modulus of each shale sample, assuming viscoelastic behavior [65]:

$$\sum_{i}^{n} \frac{1}{1+0.5\left(\frac{C_i}{C_n}-1\right)} = \sum_{i}^{n} \frac{\frac{C_i}{C_n}}{1+0.5\left(\frac{C_i}{C_n}-1\right)} \tag{26}$$

where C_i represents the creep modulus of nanoindentation and C_n represents the creep modulus of the upscaled sample.

Creep modulus values were also determined in triaxial tests (C_t) and compared with those post-nanoindentation scaling (C_n). Figure 11 illustrates a comparison of creep contact moduli obtained from both methods under differential stress. The creep modulus after scaling up shows a comparable magnitude to the triaxial test creep modulus, though some discrepancies exist, consistent with observations by Mighani et al. [46]. These differences may stem from variations in the nanoindentation test area size, potentially introducing errors in the comprehensive statistical analysis of mechanical properties at the microscopic scale. Additionally, it was noted that the creep modulus value increases with higher deviatoric stress in the triaxial test, indicating variations likely due to changes in creep strain values. It is acknowledged that both the triaxial creep modulus (C_t) and the nanoindentation-derived modulus (C_i) are stress-dependent. The upscaling approach presented here relies on the assumption of a representative average stress state. We recognize that the point load in nanoindentation does not directly translate into a triaxial stress; thus, uncertainties remain in the upscaling of creep properties. In summary, while using a single point load P in nanoindentation is a simplification that introduces uncertainty, it allows us to capture the overall trend of creep behavior from the microscale to the macroscale. We acknowledge this limitation and suggest that further research is needed to refine the stress conversion between nanoindentation tests and triaxial conditions.

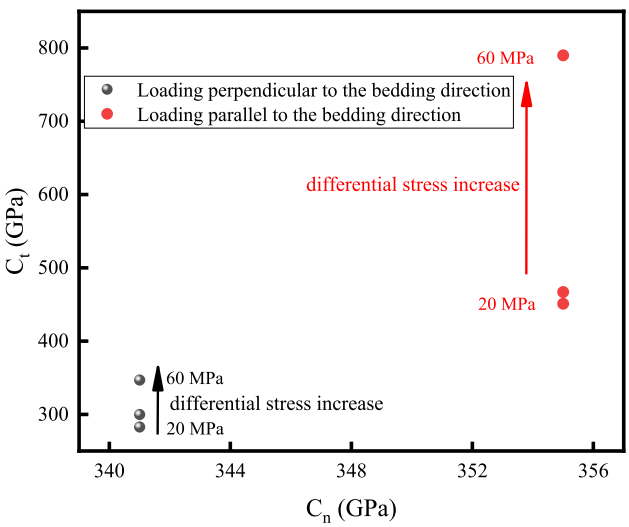

Fig. 11 Comparison of C_t and C_n at separate differential stresses

4.3 Comparisons with previous work

4.3.1 Deformation modulus

A statistical analysis was performed on the modulus results obtained from cluster analysis. Figure 12 presents the statistical distribution of elastic modulus values for each rock sample. Specifically, quartz shows a concentration within the range of 52 to 72 GPa, clay ranges from 40 to 52 GPa, calcite ranges between 60 and 87 GPa, dolomite between 83 and 108 GPa, and pyrite between 133 and 151 GPa. The measured clay content is indeed lower than that of other minerals; however, the high modulus values observed for the clay phase are consistent with previous studies [57]. Repeated experiments and rigorous statistical analysis confirm the reliability of these results. Table 6 summarizes the modulus values of common minerals in shale. Due to the heterogeneity of shale samples, mechanical parameters of individual phases exhibit significant variations. Cluster analyses revealed consistent matches between mineral phases and existing literature. Consequently, determining the mechanical properties of shale mineral components through macroscopic experiments remains challenging. Nevertheless, the proposed method offers a more comprehensive understanding of multiscale mechanical properties.

Table 6 Nanoindentation modulus measurements of shale mineral components

Component	Modulus (GPa)	Sources
Quartz	55–86	Priyavrat et al. [53] Vikas et al. [66] Ilinov et al. [24] Broz et al. [6] Ma et al. [42] Eliyahu et al. [19]
Clay minerals	32–73.9	Shi et al. [57] Kim et al. [28]
Calcite	58–90.3	Priyavrat et al. [53] Vikas et al. [66] Broz et al. [6] Eliyahu et al. [19] Shi et al. [57]
Dolomite	80.2–125.5	Kim et al. [28] Prasad et al. [52]
Pyrite	88.2–297	Priyavrat et al. [53] Vikas et al. [66] Kim et al. [28]

4.3.2 Elastic anisotropy

Ultimately, the impact of anisotropy on elastic modulus and creep is expected to be significant. Mechanical experiments were conducted at various loading angles, revealing diverse levels of elastic anisotropy across different scales within shale. Table 7 summarizes the anisotropy ratio of different constituent phases under two distinct loading directions using nanoindentation. Shale components exhibit notable anisotropy, in line with findings from Wu [68]. Additionally, the anisotropy ratio of shale at the core scale was examined and compared with published results, presented in Table 8. The core-scale anisotropy ratio of shale exceeds that of its microscopic components. Given the lamellar structure of shale, compression of bedding and fractures is facilitated in uniaxial or triaxial experiments conducted under loading

Table 7 Anisotropy ratio of modulus of mineral components in shale under different loading directions

Shale component	Modulus (GPa)		Anisotropy ratio R
	Perpendicular	Parallel	
Quartz	57.6	64.1	1.11
Clay	42.7	47.2	1.1
Calcite	68.67	84.1	1.22
Dolomite	92.8	101.7	1.09
Pyrite	161.8	137.4	0.85

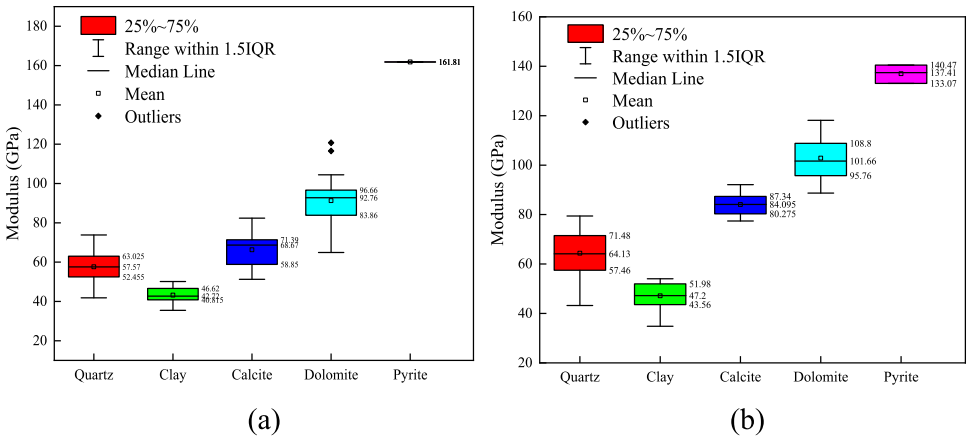

Fig. 12 Statistics of modulus for each mineral (**a**) loading perpendicular to bedding direction, (**b**) loading parallel to bedding direction

Table 8 Anisotropy ratio of modulus in shale macroscopic samples

Shale	Modulus(GPa)			Reference
	Perpendicular	Parallel	Anisotropy ratio R	
Longmaxi	24.4	30.3	1.24	Our work
Baxter	18.9	31.5	1.67	Higgins et al. [21]
Eagle Ford	23	34.6	1.50	Mokhatari et al. [47]
Floyd	25.7	44.8	1.74	Sondergeld and Rai [60]
Greenhorn	17.9	27	1.51	Jones and Wang [27]
New Albany	18.9	33.5	1.77	Johnston et al. [26]
Boyeong	19	39.3	2.07	Cho et al. [11]
Chicopee	55.8	69.2	1.24	Lo et al. [41]

perpendicular to bedding, resulting in an amplified anisotropy ratio.

4.3.3 Comparative analysis of elastic modulus from nanoindentation and triaxial compression tests

Shale, a complex rock containing various minerals, shows significant variation in mechanical properties among its components. Nanoindentation is a key technique in determining the micromechanical parameters of shale, but the complexity of its mineral composition is often overlooked in micromechanical analysis of properties. Previous research has tended to simplify the classification of shale into categories of soft, hard and intermediate minerals, ignoring the subtle differences in mechanical properties among components [1]. To bridge this gap, the correlation between micromechanical parameters and shale components was established by integrating a Gaussian mixture model with the XRD results, also taking into account the effect of mineral composition complexity on macroscopic mechanics. Additionally, the influence of the shape of various minerals on the micromechanical parameters of shale was also explored.

Scale upgrading is a critical method for relating micromechanical parameters to macromechanical parameters. The Mori–Tanaka (MT) method [49] and the self-consistent scheme (SCS) method [22] are commonly used for scaling up micromechanical observations. In the SCS method, the inclusion within the homogeneous medium is described as a granular structure [2], in contrast to the matrix inclusion morphology in the MT scheme, which does not feature a dominant phase. During the elastic scale upgrading process, different components display varying dominant phases due to differences in volume fraction and mechanical properties. Therefore, MT and SCS techniques were applied for elasticity and creep, respectively, while thoroughly considering the complexity of shale and the influence of its microstructure. The contact creep modulus obtained from nanoindentation was compared with that derived from triaxial compression testing. It was found that the contact creep modulus from nanoindentation was higher than that from triaxial testing, but the subsequent application of the SCS method brought both parameters to the same order of magnitude.

4.4 Limitations and suggestions for further work

4.4.1 Limitations

Despite the highly constrained analysis conducted in this study, it is important to recognize several limitations. First, the extent of the scaled-up approach is considered. Two types of tests are utilized to assess mechanical properties at the nanoscale (nm) and mesoscale (cm). A novel approach for scaling up is suggested to correlate the characteristics at these scales. However, the variability within shale formations across broader geological contexts may not be entirely captured. Second, the applicability of the Gaussian assumption may be examined. The Gaussian mixture-based cluster analysis is utilized to categorize the extensive nanoindentation data into different mineral groups. Nonetheless, the Gaussian assumption may not accurately reflect the mechanical properties of specific minerals. Third, the experimental conditions are addressed. Both nanoindentation and triaxial experiments are performed on dry samples at room temperature. The actual in situ conditions, such as temperature and water saturation, which undoubtedly influence mechanical properties, are not accounted for in the experiments. It should be noted that the current study is focused on the elastic properties of shale. The plastic or irreversible deformation behavior, while important, is not investigated here and represents a direction for future research.

4.4.2 Further work

To address the identified limitations, several recommendations for future work are proposed. First, the method of upgrading between sample scale and reservoir scale is to be improved. The current upscaled approach links the mechanical properties from the mineral scale to the core scale. It is suggested that reservoir characteristics, such as natural fractures, large pores and other distinct geological features, be included to further upscale the approach to reservoir scale. Second, the replication of the reservoir

environment is necessary. Both microscopic nanoindentation experiments and mesoscopic triaxial experiments should be conducted under conditions that closely mimic the reservoir environment. For the triaxial experiments, an independent flow/pressure-control system could adjust water saturation in the core sample. The sample could be immersed initially to replicate varied water saturation conditions before conducting the nanoindentation test. However, replicating the in situ temperature conditions for the nanoindentation test remains challenging. Third, advanced classification methods are recommended. The current method, based on cluster analysis, classifies the extensive measured data into several mineral groups with a substantial proportion of the mineral accounts. There is an urgent need for more advanced classification methods to enhance the accuracy and efficiency of the classification process. In addition, the researchers [5, 39, 72] have examined irreversible deformation in shales, indicating that plastic behavior is an important factor for comprehensive mechanical characterization. Future work will extend the current elastic-focused approach to include such phenomena.

5 Conclusions

Nanoindentation and triaxial creep experiments were conducted on Longmaxi shale to examine the creep behavior at both micro- and macroscales. Subsequently, cluster analysis was employed to categorize the numerous nanoindentations into corresponding mineral phases. Utilizing the microstructural data obtained from TIMA, the classical Mori–Tanaka method was modified to effectively upscale the micromechanical properties to the macroscale. The following conclusions can be drawn:

(1) Elastic and creep behaviors at the microscale were derived from the load-depth curve. The findings indicate anisotropy in the viscoelastic behavior of the shale matrix at the microscale. The modulus and creep modulus of shale minerals, when loaded parallel to bedding, are higher than those loaded perpendicular to bedding. Statistical analysis suggests that modulus and hardness of shale in both directions conform approximately to a normal distribution.

(2) The relationship between micromechanical parameters and mineral components was clarified through Gaussian mixture-based cluster analysis. The mechanical properties of each mineral component fall within a reasonable range, affirming the effectiveness of the applied classification method. Pyrite exhibits the highest modulus and creep modulus, followed by dolomite, calcite, quartz and clay. Additionally, an anisotropy ratio for different shale minerals is observed, which relates to the arrangement and geometric shapes of the minerals.

(3) The classical Mori–Tanaka method, modified with a shape factor, was utilized to upscale the elasticity accurately to the sample scale. The resulting value is closer to, yet slightly higher than, the triaxial test value. This deviation is attributed to microfracture compression during macroscopic loading. The self-consistent scheme was applied to scale up the creep modulus, and the resulting values align with the macroscale creep modulus, although the discrepancy increases with deviatoric stress.

(4) This study introduces a novel approach to classify extensive measured data into mineral phases and to then accurately upscale the micromechanical properties on a larger scale. The proposed method could potentially be applicable to other rock types and composite materials. A more precise classification method is urgently required. Moreover, both micro- and macroscale experiments, simulating conditions close to the reservoir environment, should be conducted in future work.

Acknowledgements This work is a partial result of funding by the National Key Research and Development Program of China (No. 2021YFC2902101), National Natural Science Foundation of China (Grant No. 12002081), and '111' project (B17009). DE gratefully acknowledges support from the G. Albert Shoemaker endowment.

Author contributions Cheng Wangxing was involved in writing—original draft, software, data curation. Cui Guanglei helped in writing—review and editing, conceptualization. Elsworth Derek contributed to validation, supervision. Tan Yuling was involved in methodology. Pan Zhejun helped in funding acquisition. Guo Yingjie contributed to data curation. Zhang Yu helped in methodology.

Declarations

Conflict of interest The authors declare that there are no conflicts of interest regarding the publication of this article.

References

1. Abdallah Y, Vandamme M, Chateau C, Garnier D, Jolivet I, Onaisi A, Richard D, Zandi S (2023) Linking elastic properties of various carbonate rocks to their microstructure by coupling nanoindentation and SEM-EDS. Int J Rock Mech Min Sci 170:105456. https://doi.org/10.1016/j.ijrmms.2023.105456
2. Abedi S, Slim M, Ulm F-J (2016) Nanomechanics of organic-rich shales: the role of thermal maturity and organic matter content on texture. Acta Geotech 11:775–787. https://doi.org/10.1007/s11440-016-0476-2
3. Alstadt KN, Katti KS, Katti DR (2015) Nanoscale morphology of kerogen and in situ nanomechanical properties of green river oil

shale. J Nanomechanics Micromech 6:04015003. https://doi.org/10.1061/(ASCE)NM.2153-5477.0000103
4. Bennett KC, Berla LA, Nix WD, Borja RI (2015) Instrumented nanoindentation and 3D mechanistic modeling of a shale at multiple scales. Acta Geotech 10:1–14. https://doi.org/10.1007/s11440-014-0363-7
5. Borja RI, Yin Q, Zhao Y (2020) Cam-clay plasticity. Part IX: on the anisotropy, heterogeneity, and viscoplasticity of shale. Comput Methods Appl Mech Eng. https://doi.org/10.1016/j.cma.2019.112695
6. Broz ME, Cook RF, Whitney DL (2006) Microhardness, toughness, and modulus of Mohs scale minerals. Am Mineral 91:135–142. https://doi.org/10.2138/am.2006.1844
7. Chen K, Yang R, Bao H, Dong T, Jia A, Hu Q, Guo X, He S (2023) Depositional-diagenetic process and their implications for pore development of Wufeng-Longmaxi shales in the Jiangdong block, Fuling shale gas field, SW China. Mar Pet Geol. https://doi.org/10.1016/j.marpetgeo.2023.106177
8. Chen S, Han Y, Fu C, Zhu Y, Zuo Z (2016) Micro and nano-size pores of clay minerals in shale reservoirs: implication for the accumulation of shale gas. Sediment Geol 342:180–190. https://doi.org/10.1016/j.sedgeo.2016.06.022
9. Cheng W, Cui G, Tan Y, Elsworth D, Wang C, Yang C, Chen T, Jiang C (2024) A multi-layer nanocased model to explain the U-shaped evolution of shale gas permeability at constant confining pressure. Fuel 359:130478. https://doi.org/10.1016/j.fuel.2023.130478
10. Cheng W, Guo Y, Cui G, Elsworth D, Tan Y, Pan Z (2025) Impact of micro-scale characteristics of shale reservoirs on gas depletion behavior: a microscale discrete model. Adv Geo-Energy Res 15:143–157. https://doi.org/10.46690/ager.2025.02.06
11. Cho J-W, Kim H, Jeon S, Min K-B (2012) Deformation and strength anisotropy of Asan gneiss, Boryeong shale, and Yeoncheon schist. Int J Rock Mech Min Sci 50:158–169. https://doi.org/10.1016/j.ijrmms.2011.12.004
12. Cui G, Liu J, Wei M, Shi R, Elsworth D (2018) Why shale permeability changes under variable effective stresses: new insights. Fuel 213:55–71. https://doi.org/10.1016/j.fuel.2017.10.068
13. Cui G, Tan Y, Chen T, Feng X-T, Elsworth D, Pan Z, Wang C (2020) Multidomain two-phase flow model to study the impacts of hydraulic fracturing on shale gas production. Energy Fuels 34:4273–4288. https://doi.org/10.1021/acs.energyfuels.0c00062
14. Cui G, Xia-Ting F, Pan Z, Chen T, Liu J, Elsworth D, Tan Y, Wang C (2020) Impact of shale matrix mechanical interactions on gas transport during production. J Petrol Sci Eng 184:106524. https://doi.org/10.1016/j.petrol.2019.106524
15. Dempster AP, Laird NM, Rubin DB (1977) Maximum likelihood from incomplete data via the EM algorithm. J Roy Stat Soc: Ser B (Methodol) 39:1–22. https://doi.org/10.1111/j.2517-6161.1977.tb01600.x
16. Dong G, Chen P (2017) A comparative experiment investigate of strength parameters for Longmaxi shale at the macro-and mesoscales. Int J Hydrogen Energy 42:20082–20091. https://doi.org/10.1016/j.ijhydene.2017.05.240
17. Du J, Luo S, Hu L, Guo B, Guo D, Zhang G (2022) Multiscale mechanical properties of shales: grid nanoindentation and statistical analytics. Acta Geotech 17:339–354. https://doi.org/10.1007/s11440-021-01312-8
18. Du J, Whittle AJ, Hu L, Divoux T, Meegoda JN (2021) Characterization of meso-scale mechanical properties of Longmaxi shale using grid microindentation experiments. J Rock Mech Geotech Eng 13:555–567. https://doi.org/10.1016/j.jrmge.2020.09.009
19. Eliyahu M, Emmanuel S, Day-Stirrat RJ, Macaulay CI (2015) Mechanical properties of organic matter in shales mapped at the nanometer scale. Mar Pet Geol 59:294–304. https://doi.org/10.1016/j.marpetgeo.2014.09.007
20. Graham S, Rouainia M, Aplin A, Cubillas P, Fender T, Armitage P (2021) Geomechanical characterisation of organic-rich calcareous shale using AFM and nanoindentation. Rock Mech Rock Eng 54:303–320. https://doi.org/10.1007/s00603-020-02261-6
21. Higgins S, Goodwin S, Donald A, Bratton T, Tracy G Anisotropic stress models improve completion design in the Baxter Shale. In: Higgins S, Goodwin S, Donald A, Bratton T, Tracy G (eds) SPE Annual Technical Conference and Exhibition, 2008. SPE, pp SPE-115736-MS. https://doi.org/10.2118/115736-MS
22. Hill R (1965) A self-consistent mechanics of composite materials. J Mech Phys Solids 13:213–222. https://doi.org/10.1016/0022-5096(65)90010-4
23. Hu C, Li Z (2015) A review on the mechanical properties of cement-based materials measured by nanoindentation. Constr Build Mater. https://doi.org/10.1016/j.conbuildmat.2015.05.008
24. Ilinov A (2015) Molecular dynamics simulation of elastic and sputtering properties of nanowires. University of Helsinki, Place Published
25. Javadpour F, Moravvej Farshi M, Amrein M (2012) Atomic-force microscopy: a new tool for gas-shale characterization. J Can Pet Technol 51:236–243. https://doi.org/10.2118/161015-PA
26. Johnston JE, Christensen NI (1995) Seismic anisotropy of shales. J Geophys Res: Solid Earth 100:5991–6003. https://doi.org/10.1111/j.1365-2478.2005.00495.x
27. Jones LE, Wang HF (1981) Ultrasonic velocities in Cretaceous shales from the Williston basin. Geophysics 46:288–297. https://doi.org/10.1190/1.1441199
28. Kim HJ, Kim DE (2012) Effects of Proximity on Hardness and Elastic Modulus Measurements of SiO2 and Cu by Nanoindentation. Tribol Lett 49:85–94. https://doi.org/10.1007/s11249-012-0050-5
29. Kong L, Hadavimoghaddam F, Li C, Liu K, Liu B, Semnani A, Ostadhassan M (2021) AFM vs. Nanoindentation: Nanomechanical properties of organic-rich Shale. Mar Pet Geol 132:105229. https://doi.org/10.1016/j.marpetgeo.2021.105229
30. Kumar V, Curtis ME, Gupta N, Sondergeld CH, Rai CS Estimation of elastic properties of organic matter and Woodford shale through nano-indentation measurements. In: SPE Canada Unconventional Resources Conference, 2012. SPE, pp SPE-162778-MS. https://doi.org/10.2118/162778-MS
31. Kumar V, Sondergeld CH, Rai CS Nano to macro mechanical characterization of shale. In: Kumar V, Sondergeld CH, Rai CS (eds) SPE Annual Technical Conference and Exhibition, 2012. SPE, pp SPE-159804-MS. https://doi.org/10.2118/159804-MS
32. Li C, Ostadhassan M, Abarghani A, Fogden A, Kong L (2019) Multi-scale evaluation of mechanical properties of the Bakken shale. J Mater Sci 54:2133–2151. https://doi.org/10.1007/s10853-018-2946-4
33. Li C, Ostadhassan M, Kong L, Bubach B (2019) Multi-scale assessment of mechanical properties of organic-rich shales: a coupled nanoindentation, deconvolution analysis, and homogenization method. J Petrol Sci Eng 174:80–91. https://doi.org/10.1016/j.petrol.2018.10.106
34. Li J, Wang M, Jiang C, Lu S, Li Z (2022) Sorption model of lacustrine shale oil: Insights from the contribution of organic matter and clay minerals. Energy. https://doi.org/10.1016/j.energy.2022.125011
35. Liang C, Jiang Z, Zhang C, Guo L, Yang Y, Li J (2014) The shale characteristics and shale gas exploration prospects of the Lower Silurian Longmaxi shale, Sichuan Basin, South China. J Nat Gas Sci Eng 21:636–648. https://doi.org/10.1016/j.jngse.2014.09.034

36. Liu K, Ostadhassan M, Bubach B (2016) Applications of nanoindentation methods to estimate nanoscale mechanical properties of shale reservoir rocks. J Nat Gas Sci Eng 35:1310–1319. https://doi.org/10.1016/j.jngse.2016.09.068
37. Liu K, Ostadhassan M, Bubach B (2018) Application of nanoindentation to characterize creep behavior of oil shales. J Petrol Sci Eng 167:729–736. https://doi.org/10.1016/j.petrol.2018.04.055
38. Liu K, Rassouli FS, Liu B, Ostadhassan M (2021) Creep behavior of shale: Nanoindentation vs. triaxial creep tests. Rock Mech Rock Eng 54:321–335. https://doi.org/10.1007/s00603-020-02255-4
39. Liu Y, Burch AC, Bennett KC, Abousleiman Y, Borja RI (2023) Bridging nanoindentation and triaxial creep tests on a shale. Acta Geotech 18:6475–6487. https://doi.org/10.1007/s11440-023-02133-7
40. Liu Y, Wu B, Gong Q, Cao H (2019) Geochemical characteristics of the lower Silurian Longmaxi Formation on the Yangtze Platform, South China: Implications for depositional environment and accumulation of organic matters. J Asian Earth Sci. https://doi.org/10.1016/j.jseaes.2019.104003
41. Lo T-w, Coyner KB, Toksoz MN (1986) Experimental determination of elastic anisotropy of Berea sandstone, Chicopee shale, and Chelmsford granite. Geophysics 51:164–171. https://doi.org/10.1190/1.1442029
42. Ma Z, Gamage RP, Zhang C (2021) Mechanical properties of α-quartz using nanoindentation tests and molecular dynamics simulations. Int J Rock Mech Min Sci. https://doi.org/10.1016/j.ijrmms.2021.104878
43. Ma Z, Pathegama Gamage R, Zhang C (2020) Application of nanoindentation technology in rocks: a review. Geomech Geophys Geo-Energy Geo-Resour. https://doi.org/10.1007/s40948-020-00178-6
44. McLachlan GJ, Basford KE (1988) Mixture models: Inference and applications to clustering, vol 38. M. Dekker New York, New York
45. Metwally YM, Chesnokov EM (2012) Clay mineral transformation as a major source for authigenic quartz in thermo-mature gas shale. Appl Clay Sci 55:138–150. https://doi.org/10.1016/j.clay.2011.11.007
46. Mighani S, Bernabé Y, Boulenouar A, Mok U, Evans B (2019) Creep deformation in Vaca Muerta shale from nanoindentation to triaxial experiments. J Geophys Res: Solid Earth. https://doi.org/10.1029/2019JB017524
47. Mokhtari M, Honarpour MM, Tutuncu AN, Boitnott GN (2016) Characterization of elastic anisotropy in Eagle Ford Shale: Impact of heterogeneity and measurement scale. SPE Reservoir Eval Eng 19:429–439. https://doi.org/10.2118/170707-PA
48. Moon TK (1996) The expectation-maximization algorithm. IEEE Signal Process Mag 13:47–60. https://doi.org/10.1109/79.543975
49. Mori T, Tanaka K (1973) Average stress in matrix and average elastic energy of materials with misfitting inclusions. Acta Metall 21:571–574. https://doi.org/10.1016/0001-6160(73)90064-3
50. Mukherjee R, Misra S (2023) Nanomechanics of minerals: understandings and developments through instrumented nanoindentation techniques. Phys Chem Miner. https://doi.org/10.1007/s00269-023-01235-8
51. Oliver WC, Pharr GM (1992) An improved technique for determining hardness and elastic modulus using load and displacement sensing indentation experiments. J Mater Res 7:1564–1583. https://doi.org/10.1557/jmr.1992.1564
52. Prasad M, Kopycinska M, Rabe U, Arnold W (2002) Measurement of Young's modulus of clay minerals using atomic force acoustic microscopy. Geophys Res Lett. https://doi.org/10.1029/2001gl014054
53. Priyavrat Shukla VK, Mark Curtis, Carl H. Sondergeld and Chandra S. Rai (2013) Nanoindentation Studies on Shales. In ARMA US Rock Mechanics/Geomechanics Symposium (pp ARMA-2013)
54. Schwartz B, Elsworth D, Marone C (2019) Relationships between mechanical and transport properties in Marcellus shale. Int J Rock Mech Min Sci 119:205–210. https://doi.org/10.1016/j.ijrmms.2019.04.020
55. Schwartz B, Huffman K, Thornton D, Elsworth D (2019) The effects of mineral distribution, pore geometry, and pore density on permeability evolution in gas shales. Fuel 257:116005. https://doi.org/10.1016/j.fuel.2019.116005
56. Schwartz B, Huffman K, Thornton D, Elsworth D (2019) A strain based approach to calculate disparities in pore structure between shale basins during permeability evolution. J Nat Gas Sci Eng 68:102893. https://doi.org/10.1016/j.jngse.2019.05.006
57. Shi X, Jiang S, Lu S, He Z, Li D, Wang Z, Xiao D (2019) Investigation of mechanical properties of bedded shale by nanoindentation tests: a case study on Lower Silurian Longmaxi Formation of Youyang area in southeast Chongqing, China. Pet Explor Dev 46:163–172. https://doi.org/10.1016/s1876-3804(19)30016-3
58. Shi X, Jiang S, Yang L, Tang M, Xiao D (2020) Modeling the viscoelasticity of shale by nanoindentation creep tests. Int J Rock Mech Min Sci. https://doi.org/10.1016/j.ijrmms.2020.104210
59. Slim MI (2016) Creep Properties of Source Rocks Using Indentation: The Role of Organic Matter on Texture and Creep Rates. Massachusetts Institute of Technology, Department of Earth, Atmospheric., Cambridge, Massachusetts.
60. Sondergeld CH, Rai CS (2011) Elastic anisotropy of shales. Lead Edge 30:324–331. https://doi.org/10.1190/1.3567264
61. Sone H, Zoback MD (2013) Mechanical properties of shale-gas reservoir rocks—Part 2: Ductile creep, brittle strength, and their relation to the elastic modulus. Geophysics 78:D393–D402. https://doi.org/10.1190/geo2013-0051.1
62. Standardization IOf (2002) Metallic Materials: Instrumented Indentation Test for Hardness and Materials Parameters. Test Method. ISO 14577–1:2015(E).
63. Sun Z, Elsworth D, Cui G, Li Y, Zhu A, Chen T (2024) Impacts of rate of change in effective stress and inertial effects on fault slip behavior: new insights into injection-induced earthquakes. J Geophys Res: Solid Earth 129:e2023JB027126. https://doi.org/10.1029/2023JB027126
64. Vandamme M, Tweedie CA, Constantinides G, Ulm F-J, Van Vliet KJ (2011) Quantifying plasticity-independent creep compliance and relaxation of viscoelastoplastic materials under contact loading. J Mater Res 27:302–312. https://doi.org/10.1557/jmr.2011.302
65. Vandamme M, Ulm FJ (2013) Nanoindentation investigation of creep properties of calcium silicate hydrates. Cem Concr Res. https://doi.org/10.1016/j.cemconres.2013.05.006
66. Vikas Kumar CHS, and Chandra S. Rai (2012) Nano to Macro Mechanical Characterization of Shale. SPE Annual Technical Conference and Exhibition: SPE-159804-MS. https://doi.org/10.2118/159804-MS
67. Wu T, Zhao J, Zhang W, Zhang D (2020) Nanopore structure and nanomechanical properties of organic-rich terrestrial shale: An insight into technical issues for hydrocarbon production. Nano Energy. https://doi.org/10.1016/j.nanoen.2019.104426
68. Wu Y, Li Y, Luo S, Lu M, Zhou N, Wang D, Zhang G (2020) Multiscale elastic anisotropy of a shale characterized by cross-scale big data nanoindentation. Int J Rock Mech Min Sci. https://doi.org/10.1016/j.ijrmms.2020.104458
69. Xu T, Heng Z, Liu B, Heap MJ, Wasantha PLP, Li Z (2024) A microscopic approach to brittle creep and time-dependent

fracturing of rocks based on stress corrosion model. Deep Resour Eng. https://doi.org/10.1016/j.deepre.2024.100111
70. Yang C, Xiong Y, Wang J, Li Y, Jiang W (2020) Mechanical characterization of shale matrix minerals using phase-positioned nanoindentation and nano-dynamic mechanical analysis. Int J Coal Geol 229:103571. https://doi.org/10.1016/j.coal.2020.103571
71. Yi-Kai G, Zhen-Kui J, Jian-Hua Z, Xin W, Zhen-Peng Z, Yang W (2018) Clay minerals in shales of the Lower Silurian Longmaxi Formation in the Eastern Sichuan Basin, China. Clay Miner 52:217–233. https://doi.org/10.1180/claymin.2017.052.2.04
72. Yin Q, Liu Y, Borja RI (2021) Mechanisms of creep in shale from nanoscale to specimen scale. Comput Geotech. https://doi.org/10.1016/j.compgeo.2021.104138
73. Zargari S, Wilkinson TM, Packard CE, Prasad M (2016) Effect of thermal maturity on elastic properties of kerogen. Geophysics 81:M1–M6. https://doi.org/10.1190/geo2015-0194.1
74. Zeng L, Akhondzadeh H, Iqbal MA, Keshavarz A, Rezaee R, Xie Q (2022) Effect of fluid-shale interactions on shales micromechanics: Nanoindentation experiments and interpretation from geochemical perspective. J Nat Gas Sci Eng 101:104545. https://doi.org/10.1016/j.jngse.2022.104545
75. Zou C (2017) Unconventional petroleum geology. Elsevier